Numerical study of elastic-plastic behaviour of pore-containing materials: effects of pore arrangement

Yu-Lin Shen* and Nima Fathi

Department of Mechanical Engineering,
University of New Mexico,
Albuquerque, NM 87131, USA
Email: shenyl@unm.edu
Email: nfathi@unm.edu
*Corresponding author

Abstract: The present investigation aims to evaluate the elastic and plastic behaviour of porous materials through micromechanical modelling. Nonlinear computational analyses were conducted using the finite element method (FEM). The effective elastic and plastic behaviours of the model structures, encompassing a range of porosity up to 20% with various pore geometries, were investigated. Attention is directed to the uniaxial stress-strain response as a function of the porous microstructure. The model geometries were generated based on non-overlapping pore topologies arranged in an orderly manner. The sensitivity of the results to the pore morphology was examined by comparing the normalised effective modulus of elasticity for all cases, and was validated by the experimental data. As expected, the introduction of porosity was found to reduce the elastic modulus of the media. Also, the pore arrangement variation has a direct influence on the effective mechanical response beyond the elastic limit. In addition, stress distribution in the porous microstructure was significantly influenced by the pore morphology. The approach can be readily generalised to study a wide variety of porous solids from nano-structured materials to geological structures.

Keywords: porous material; finite element method; FEM; micromechanical modelling; elastic modulus; plastic deformation.

Biographical notes: Yu-Lin Shen received his PhD in Engineering from Brown University in 1994, and MS and BS in Materials Science and Engineering from National Tsing Hua University in Taiwan. He was a Postdoctoral Research Associate at the Massachusetts Institute of Technology before joining University of New Mexico (UNM), in 1996. He is currently Professor and Chair in the Department of Mechanical Engineering at UNM. He has been active in research and teaching in the areas of mechanical behaviour of materials and solid mechanics. He is particularly well versed in applying modelling techniques to address micro-mechanical problems related to thin films, microelectronic devices and packages, and composite materials. He has published about 200 research papers, mostly in the form of journal articles. His book titled *Constrained Deformation of Materials* was published by Springer, in 2010. He is an elected Fellow of the American Society of Mechanical Engineers (ASME).

Nima Fathi holds a BS in Mechanical Engineering and MS in Mechanical Engineering. His secondary MS is in Nuclear Engineering, and he received his PhD in Mechanical Engineering from the University of New Mexico (UNM). He currently serves academia as a Research Assistant Professor at the Mechanical Engineering Department of UNM. He is the Interim Chair of the American Nuclear Society (ANS) 10.4 Working Group, Verification and Validation (V&V) of Non-safety-related Scientific and Engineering Computer Programs for the Nuclear Industry and technical member of ASME V&V 20 Codes and Standards Committee, V&V in Computational Fluid Dynamics and Heat Transfer.

1 Introduction

Recent developments in technology have created an exponentially increasing demand for investigating the effective physical properties of composite and heterogeneous materials (Kaviany, 1995). It is observed that heterogeneity leads to more complicated physics at the scale where heterogeneity exists, making analysis and material behaviour prediction more difficult. As a result of the intricate descriptions and/or understanding of the physics required to determine the behaviour of a heterogeneous material or system, practitioners frequently prefer the use of effective properties or responses. As engineering systems become increasingly complex, it is advantageous and even necessary to use effective properties to analyse and predict system performance in a feasible manner. Heterogeneity can significantly affect the mechanical response. Therefore, it is important to evaluate the impact of heterogeneous characteristics on the mechanical behaviour either on a fine scale (e.g., at the material level) or on a larger scale (e.g., at the system level).

The effect of heterogeneity is especially important in porous materials – e.g., nuclear fuel components – where pores in the bulk material matrix impede and divert heat flow within the material and alter the mechanical properties. Porous media are two-phase composites comprising solid (matrix) and fluid (void) phases – either a gas or a liquid may occupy the void. Porous structures are ubiquitous in modern technologies (Irick and Fathi, 2019). This is especially true in energy systems such as thermal barrier coatings (Gu et al., 2001; Renteria et al., 2006; Zhu et al., 2019), semi-conductor devices (Zhao et al., 2019), energy storage materials (Dinesh and Bhattacharya, 2019), as well as the cooling channels and compact heat exchangers (Yeap et al., 2013). Another prominent application where porous materials are found is in flame retardant material development. Carbon-nanotube-based materials can exhibit excellent flame-retardant properties, potentially serving as safety and protective mechanisms in a wide variety of applications. In carbon nanofibre composites, the carbon nanotubes can act as filler materials in a bulk matrix, or can act as porous sheets protecting polymer surfaces. Mechanical and thermal advantages to doping epoxy resins with graphene nanosheets were shown by Wu et al. (2019). In addition, the thermal protection capabilities of porous carbon membranes were studied by Irick and Fathi (2020). This study used these membranes on the surface of epoxy carbon fibre composites, where the pore size of the membrane was measured as a metric in characterising the thermal performance.

The additive manufacturing technology – commonly known as 3D printing – is another main application of porous media which recently has attracted significant attention. This technology has made possible the computerised fabrication of porous

structures in various forms including foam and lattice at different scales. There is a natural need for understanding the elastic and plastic behaviours of printed porous materials, considering the non-homogeneous and high-temperature processes used (Gobetz et al., 2016; Zhang et al., 2018; Ibrahim et al., 2020). The mechanical performance of other advanced materials – such as aerogels and doped polymers – are driven by their heterogeneous characteristics and can be seen in marine, oil and gas, aerospace, energy and thermal management industries (Danes et al., 2003; Zhao et al., 2012; Wu et al., 2019). The expansive set of industries and specific thermal/mechanical applications where heterogeneous and especially porous materials are of immediate consequence is immeasurable. Thus, the pursuit of measuring, analysing, and predicting the nano, micro and macro-structural response of such materials is in high demand.

Mechanical properties such as elastic modulus can be affected by the variation of pore shape and distribution. There have been published works on this matter for uniform pore distributions (Digby, 1981; Sun and Li, 1988; Ramakrishnan and Arunachalam, 1990; Uppu et al., 2015; Doan et al., 2020) as well as non-uniform cases (Campillo et al., 2021; Kırca et al., 2007; Pérez et al., 2015, 2017; de Galarreta et al., 2020; Zeng et al., 2015). Here, we present the dependence of elastic modulus based on various periodic arrangements and distributions of the porous structure, and evaluate the numerical results against experimental measurements using area validation metric (AVM). The micro-mechanical modelling also extends to the effective stress-strain behaviour beyond the elastic limit. The numerical modelling only considers idealised pore configurations, but it offers physical insights into how microscopic porous geometry affects the macroscopic mechanical response through systematic analyses. The difference in arrangement and distribution of pore structures plays a key role in the optimisation of pore topology and a desired effective material property.

This paper is organised as follows. Section 2 describes the modelling approach and the computational methods. Section 3 introduces the experimental framework and our statistical validation assessment used to quantify the reliability of the computational results. Section 4 discusses the combined results on elastic behaviour from the computation and the validation analysis. The numerical analysis is extended to the plastic regime in Section 5. Finally, Section 6 summarises the major findings.

2   Modelling approach

This study focuses on periodic arrays of circular and elliptical pores under overall uniaxial loading. Figure 1(a) shows the baseline model where circular pores of uniform size are packed in a square array. The shaded circles represent the pores which are surrounded by the solid matrix. Due to periodicity and symmetry, the highlighted squares are the actual areas needed for the computational simulations, as will be described below. Tensile loading can be applied along the 0/90° directions (performed only in the *y*-direction since the result is the same as in the *x*-direction) and along the 45° direction, as shown in Figure 1(a). A different set of circular-pore models are also studied, with a mixture of large and small pores arranged in a square-periodic manner as shown in Figure 1(b). The diameter of large pores is taken as twice that of the small pores. Again, loading along the 0/90° and 45° directions can be analysed as highlighted.

Figure 1   Schematics showing (a) the square array of circular pores of uniform size and
(b) the square array of periodically mixed large and small circular pores (see online
version for colours)

(a)

(b)
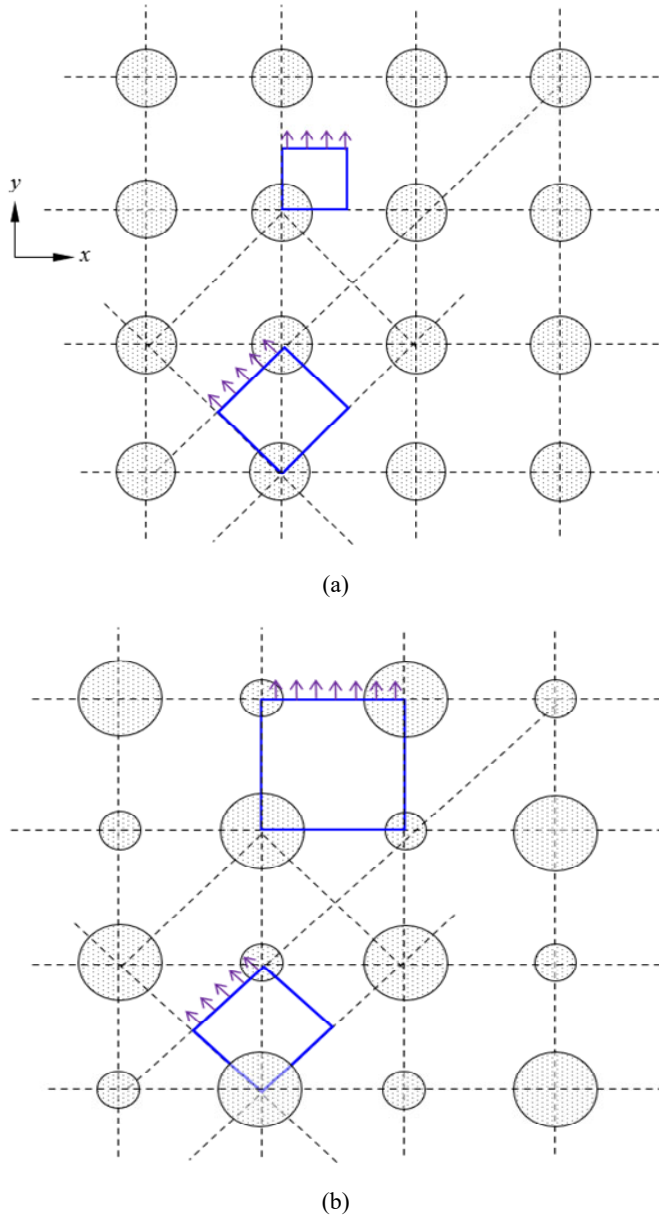
Note: The shaded circles represent the pores, and the highlighted squares are the actual
domains needed for the simulations, with the arrows representing pulling directions
for the 0/90° and 45° loading.

Figure 2   Schematics of the various elliptical pore arrangements considered in this study, (a) pores in an aligned square array (b) pores arranged in a staggered array (c) elliptic pores with mixed orientations in an aligned square array (d) elliptical pores with mixed orientation in a staggered array (see online version for colours)

(a)   (b)

(c)   (d)
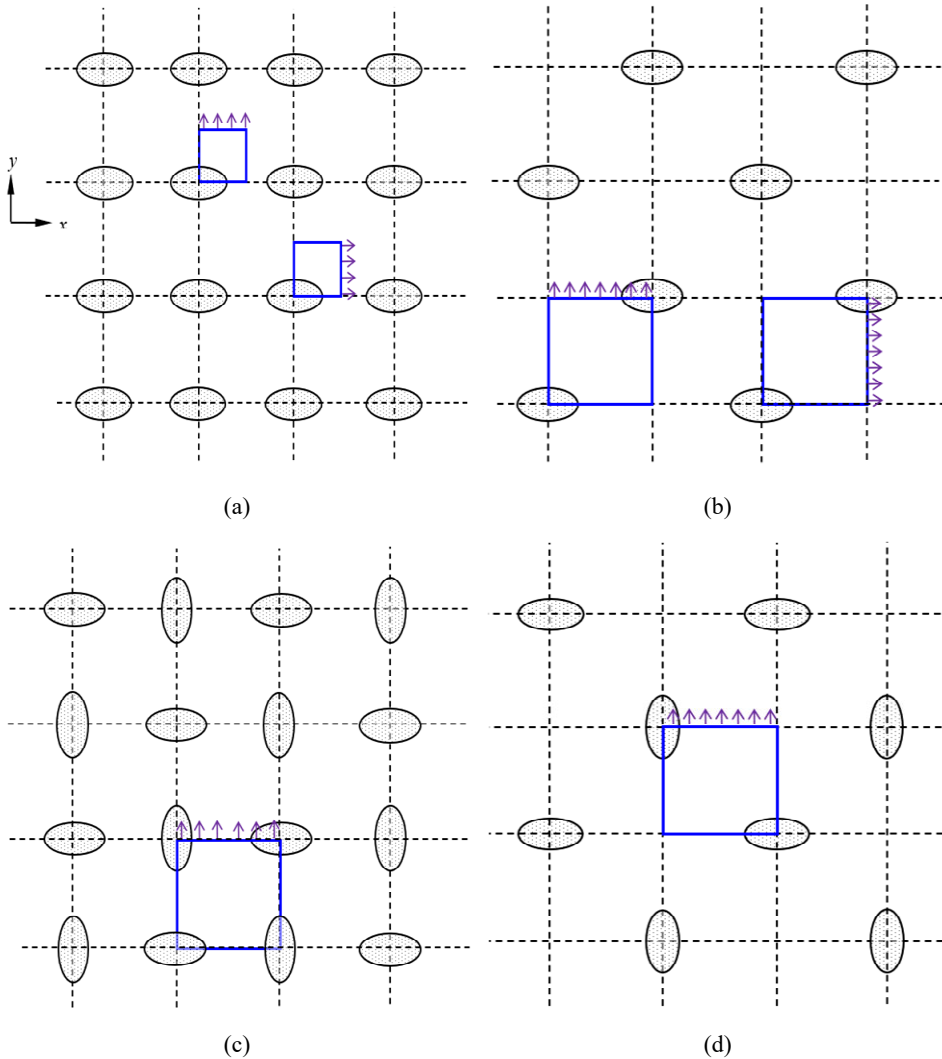
Note: The arrangements in Figures 2(a) and 2(b) give rise to anisotropic behaviour in *x* and *y*, and they are analysed separately.

To investigate the effects of pore shape with aspect ratios deviating from unity, numerical models with elliptical pores are constructed. Figures 2(a) and 2(b) show the cases where all pores have the same orientation (major axis along the *x*-direction), with Figures 2(a) and 2(b) featuring a square alignment and staggered distribution, respectively. An anisotropic mechanical response is expected, so in each configuration loading along the *x* and *y*-directions are analysed separately as highlighted in Figures 2(a) and 2(b). Figures 2(c) and 2(d) show two models where the elliptical pores have mixed orientations, resulting in the same mechanical response along the *x* and *y*-directions. In

Figures 2(c) and 2(d), the pore centres are placed in a square alignment and staggered distribution, respectively. In all the elliptical cases, the major axis of the pore is taken to be twice as long as the minor axis. Note that in the current numerical study, there is no true length scale in the models. Specifying the pore shape, spatial distribution, and overall porosity (area fraction) will uniquely determine the outcome.

The highlighted squares in Figures 1 and 2 are the actual 'unit cells' used for the calculations. Their four sides are all symmetry lines. With appropriate boundary and loading conditions imposed, a single unit cell effectively represents an infinite array of microstructures. An example of the 0/90° loading model in Figure 2(a) is shown in Figure 3(a). The bottom boundary ($y = 0$) is not allowed to displace in the y-direction but tangential slide in x is allowed, and the left boundary ($x = 0$) is not allowed to displace in the x-direction but tangential slide in y is allowed. These boundary conditions are represented in Figure 3(a) by the 'rollers'. Loading is applied to the top boundary (initially $y = L_0$) by imposing a displacement in the y-direction. The right boundary (initially $x = L_0$) can move in response to the deformation, but is constrained to remain vertical to preserve symmetry. For the 45° loading model, the boundary conditions are the same except that the x and y-axes labelled in Figure 3(a) become the two 45° directions [see the highlighted 45° domain in Figure 1(b)]. The overall engineering strain (ε) is then expressed as $(L - L_0) / L_0$, where L is the current length of the model in the y-direction. The overall engineering stress (σ) is the reaction force in y on the top boundary, obtained from the analysis, divided by the original cross-section area L_0 (taking into account of the default domain depth of unity in the z-direction for the 2D model). The overall stress-strain curves resulting from the simulations can thus be plotted. The effective elastic modulus is then $E = \sigma / \varepsilon$ at the beginning of loading.

The simulations were carried out using the finite element software ABAQUS (version 2017, Dassault Systems Simulia Corp., Johnston, RI, USA). The solid matrix is taken to be an isotropic elastic-perfectly plastic material, with Young's modulus (E_0), Poisson's ratio (v_0) and yield strength (σ_0) being 70 GPa, 0.33 and 200 MPa, respectively. While a constant set of material properties was used as input, the effective elastic modulus will be presented in a normalised form so the results can be readily applied to any linear elastic material. Although only 2D simulations are considered in this study, we performed both plane stress and plane strain analyses. Due to the mechanical constraint in plane strain, the two cases resulted in different effective elastic moduli, with the values under plane strain being higher. However, when the effective modulus is normalised by the respective modulus of the matrix material, the plane stress and plane strain conditions lead to the same behaviour. Figure 3(b) shows an example, plotting the normalised effective modulus as a function of the pore concentration (defined as the area fraction of pores), using the model of circular pores of the same size under the two loading directions as in Figure 2(a). Identical results for plane stress and plane strain can be seen. It is also evident that the 0/90° loading results in a higher effective modulus than the 45° loading under a given pore concentration. More discussion about this finding will be given in Section 4. Besides the validation assessment, only the plane strain results from the computational study will be presented in the remainder of this paper. Note that from the earlier simulation works on two-phase composite materials, the plane-strain model is able to qualitatively represent the more elaborate 3D calculations well into the plastic regime of deformation (Christman et al., 1989; Llorca et al., 1991; Hom, 1992; Shen et al., 1995; Wilkins and Shen, 2001; Kozola and Shen, 2003).

Figure 3   (a) Computational domain used for the actual modelling, along with the prescribed loading and boundary conditions (b) Simulated normalised effective modulus as a function of pore area fraction, for the uniformly sized circular pore models under the 0/90° and 45° loading directions (see online version for colours)

(a)

(b)
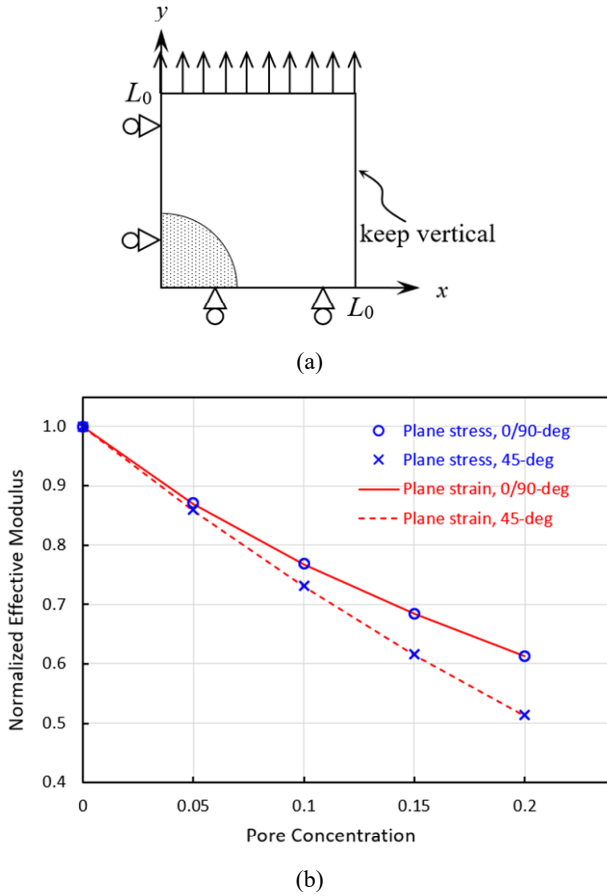
3   Validation approach

To assess the fidelity of the numerical model and achieve a better understanding of how the effective elastic modulus changes as the porosity varies, several experimental specimens were fabricated to represent a range of aligned porosity comparable to those used in the modelling. The materials were tested using material testing system (MTS) 810 (MTS Systems Corporation). Due to the specific shape and size of the specimens, the MTS-810's linear velocity displacement transducer (LVDT) was used. The LVDT is a sensor that is embedded in the crosshead of the MTS machine and measures the pressing ram displacement. Since the LVDT measures overall ram displacement, care must be exercised when picking a test material so that the displacement of the ram material does not add to the displacement of the part itself. The material used in the experiment was polycarbonate, chosen due to its availability and relatively low modulus of elasticity.

Additional stainless-steel ram extensions were added to the press to account for the small length of the test specimens. To measure the porosity level for all samples, bulk and pore volume measurements and a comparison analysis were used to estimate the porosity. The first test specimen was loaded to failure to produce a complete force-displacement curve. From this curve, it is possible to identify the linear region and apply displacement constraints to the press. The highest porosity material, being the weakest, was chosen to conduct this compression to failure. Using the result of this first test as the maximum displacement of the MTS ram, it was possible to conduct the remaining tests without introducing plastic deformation to the specimens. Figure 4(a) shows the schematic of the testing machine. Figure 4(b) presents the measured data calculated from the testing analysis for all cases.

Figure 4   (a) Schematic of the tensile/compression test (b) The normalised effective modulus calculated from the experimental data (see online version for colours)
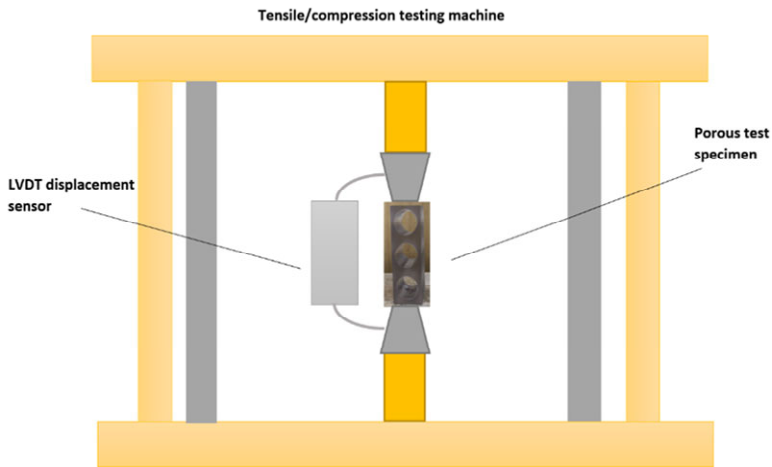
(a)
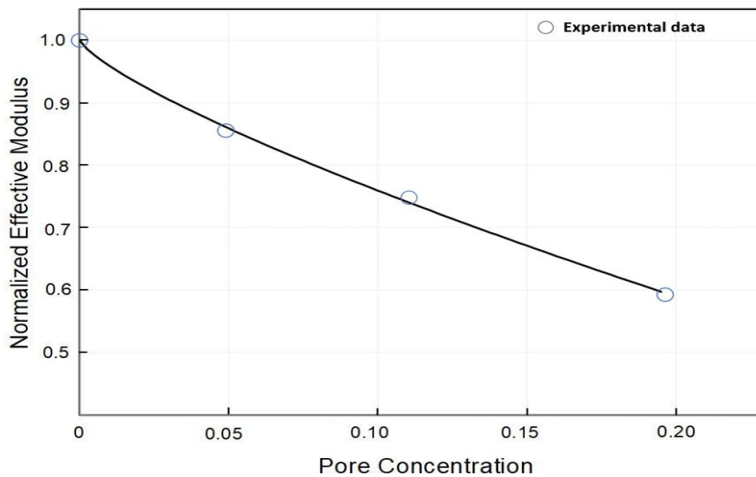
(b)

To perform a quantitative comparison between the computational results and experimental data, a modified version of the AVM method was applied (Roy and Voyles, 2013). Validation is defined as the process of determining the degree to which a computational model is an accurate representation of the real world from the perspective of the intended uses of the model. One of the steps in the validation process is a comparison of the results predicted by the model with corresponding quantities observed in the validation experiments. Therefore, an assessment of the model accuracy is obtained. Note that accuracy is measured in relation to experimental data which is considered as the best measure of reality. This strategy does not assume that the experimental measurements are more accurate than the computational results. Here, the validation metric is defined to be the area between the cumulative distribution function from the simulation and the empirical distribution function (EDF) which is also known as the empirical cumulative distribution function from the experiment. If the number of simulation samples is limited, we can represent the simulation by individual samples and use EDF for the simulation results as well. If the area between the EDF of the experiment and the EDF of simulation is 0, it means there is no evidence that the simulation and the experiment are in disagreement. In this analysis, the modified version of the AVM is applied (Oberkampf and Roy, 2010).

4   Effective elastic modulus

The numerical results of the effective elastic modulus are now presented in a similar form as Figure 3(b). Figure 5(a) shows the normalised modulus as a function of the pore concentration for the four circular pore models. In the cases of uniform pores size, the 0/90° loading results in much higher effective moduli than the 45° loading. Note that, for two-phase composite materials with stiffer particles embedded in a more compliant matrix, the 0/90° loading also leads to higher effective moduli (Shen et al., 1994; Shen, 2010). Now with the hard particles replaced by voids, the same trend still holds true. Also included in Figure 5(a) are circular pores with two different sizes. The two loading scenarios generate much closer modulus values, but the 0/90° case is still stiffer. It is worthy of mention that, if the small and large pores are made closer in size, the results will tend to those of the uniform pore size (i.e., the green solid and dashed curves will move closer to the red solid and dashed curves, respectively).

The results for the elliptical pores are shown in Figure 5(b). When the pores are oriented in the same direction, loading along the major axis of the ellipse results in a stiffer response. This is again similar to the situation if the pores are replaced by stiff short fibres. For the elliptical aspect ratio considered in this study, there is a very large difference in effective modulus between the x and y-direction loadings as seen in Figure 5(b) (difference between the solid and dashed curves in blue and the same in green). Comparing the aligned and staggered arrangements (the sets of blue and green curves, respectively), the aligned pores give rise to higher effective modulus values just like the case of circular pores. Note that this trend (aligned vs. staggered) persists when considering the mixed-orientation pore distributions as represented by the pink curves (solid vs. dashed).

Figure 5 Simulated normalised effective modulus as a function of pore area fraction for (a) the four circular pore models shown in Figure 1 and (b) the six elliptical pore models shown in Figure 2 (see online version for colours)
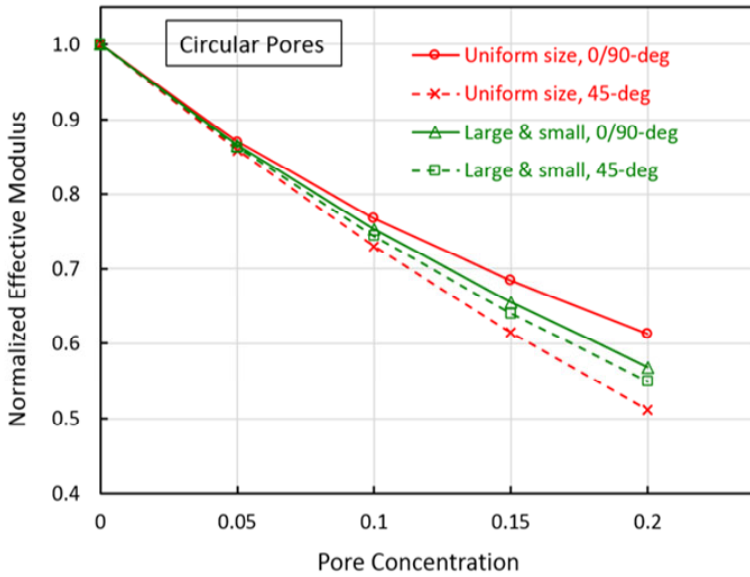
(a)
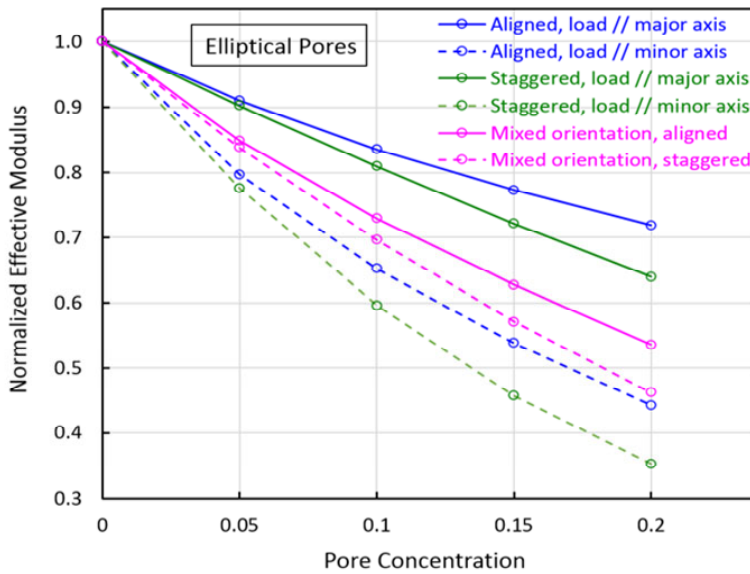
(b)

To compare the computational results against the experimental data, two approaches are applied. Figure 6 overlays the experimental data on all the aforementioned circular-pore numerical results. The simulations show good agreement with the experiments, and the uniform circular case has the least mismatch in comparison with the other cases due to

the pore geometrical difference. However, this comparison is more qualitative than quantitative. To be able to compare the simulations with the experimental results more quantitatively and statistically, the modified AVM was applied as mentioned in the previous section. This method provides the uncertainty estimation of the computational results with respect to the experimental data in the form of a probabilistic domain which is called model form uncertainty.

Figure 6   Comparison of the computational results against the experimental data for all circular pore cases (see online version for colours)
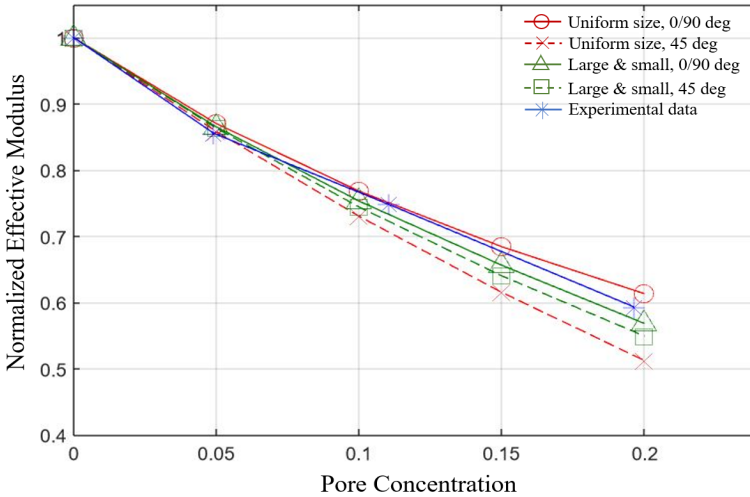
Figure 7(a) presents the mismatch between the single deterministic experimental data and the computational samples for the uniform circular pore concentration of 0.05 via empirical cumulative distribution functions. The mismatch area is designated as *d*. The coloured areas are the mismatch of experimental and simulation cumulative values. The red area represents the positive mismatch (d^+) and the blue area represents the negative mismatch (d^-) which is evaluated for the model form uncertainty. If *S* is considered as the simulation mean value or the function simulation results, the model form uncertainty can be presented as $[S - F_s d^-, S + F_s d^+]$, $F_s = 1.25$, where F_s is the factor of safety (Oberkampf and Roy, 2010).

Figure 7(b) shows the same kind of mismatch area as in Figure 7(a) but for the numerical results of large and small circular pores at the same 0.05 concentration. The two cases display considerably different mismatch areas, larger in the case of Figure 7(b). This observation corroborates with the nature of the experimental samples since they include uniform pores. Figures 8–10 show the AVMs for the pore concentration of 0.1, 0.15 and 0.2, respectively, for all the computational results of circular pores. It is observed that the mismatch increases when the uniformity changes as well as the porosity increases. Lower mismatch values were obtained for uniform circular pores since they are more compatible geometrically with the experimental samples. The model form uncertainty of all cases can be calculated and plotted, as in Figure 11, for an overall evaluation. It is evident that with an increase in pore concentration the uncertainty and mismatch increase for both uniform and non-uniform (large and small) samples.

Figure 7 Empirical cumulative probability of the experimental data and simulation results of the models with (a) uniform circular pores and (b) non-uniform (large and small) circular pores, for the case of 0.05 pore concentration (see online version for colours)
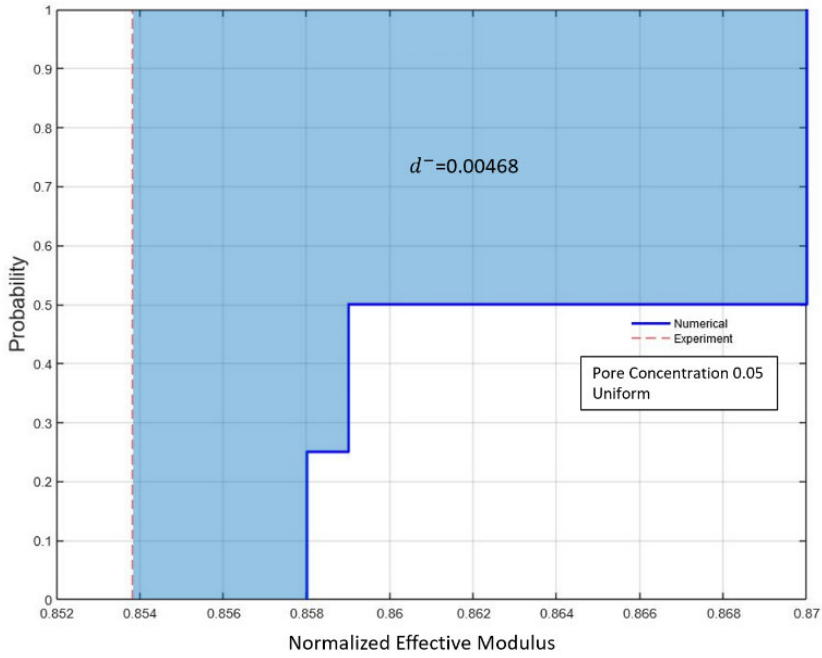
(a)
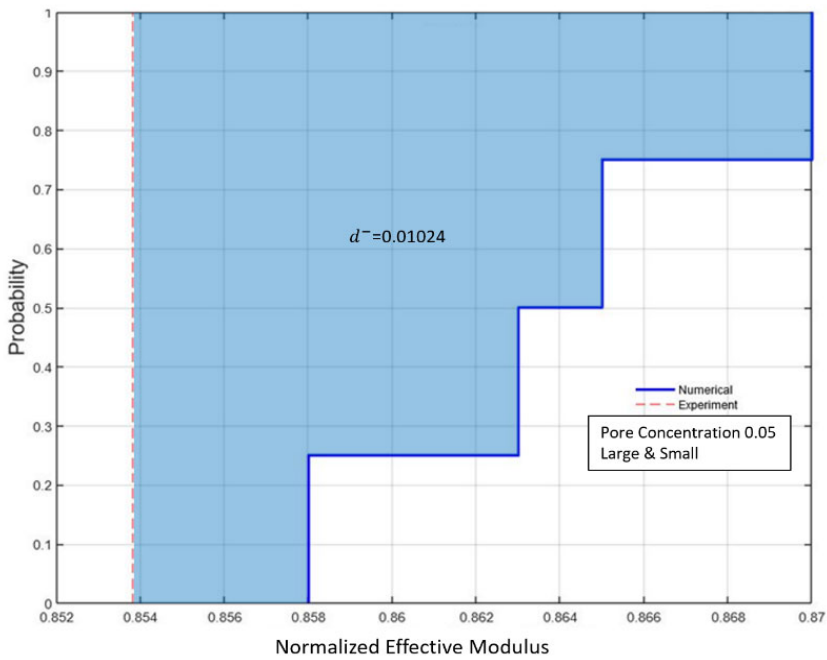
(b)

Figure 8 Empirical cumulative probability of the experimental data and simulation results of the models with (a) uniform circular pores and (b) non-uniform (large and small) circular pores, for the case of 0.10 pore concentration (see online version for colours)
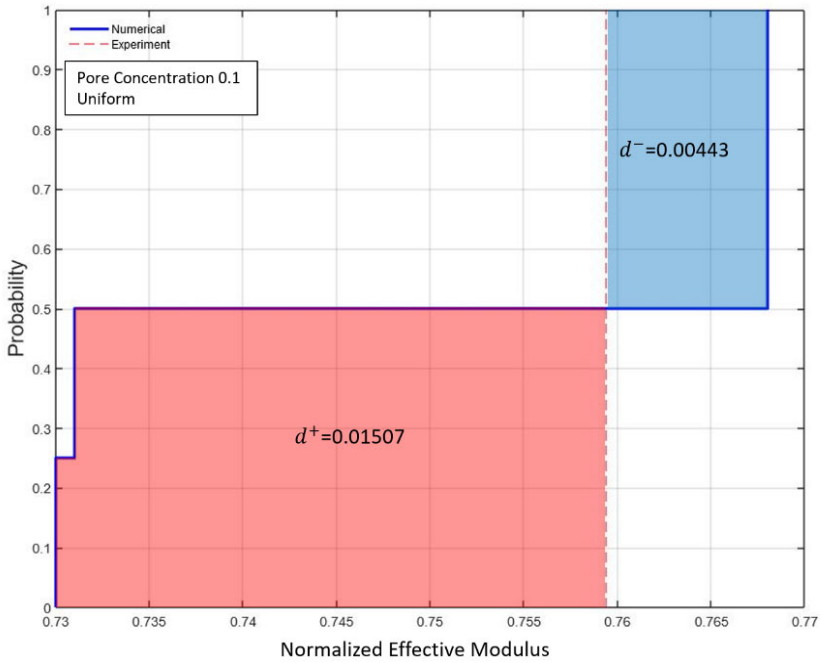
(a)
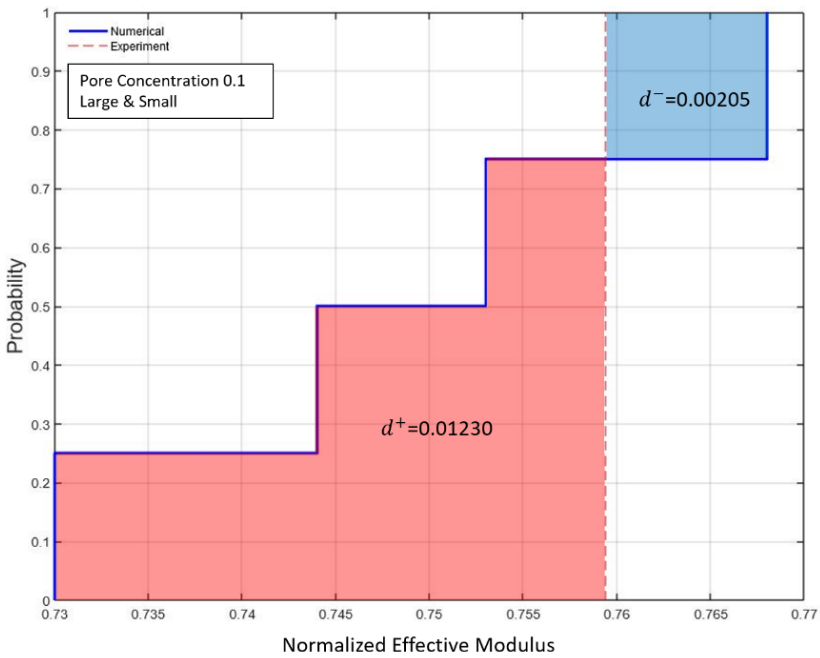
(b)

Figure 9   Empirical cumulative probability of the experimental data and simulation results of the models with (a) uniform circular pores and (b) non-uniform (large and small) circular pores, for the case of 0.15 pore concentration (see online version for colours)
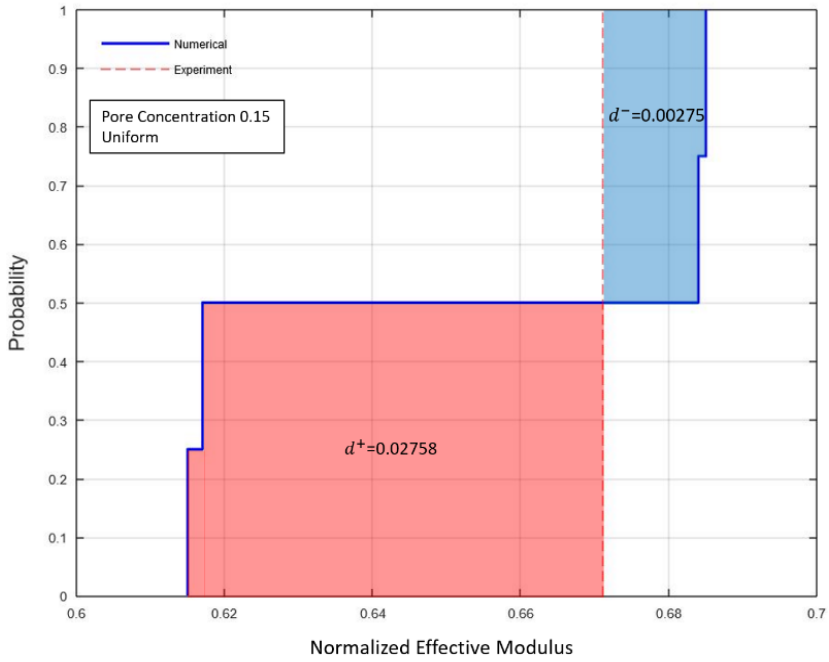
(a)
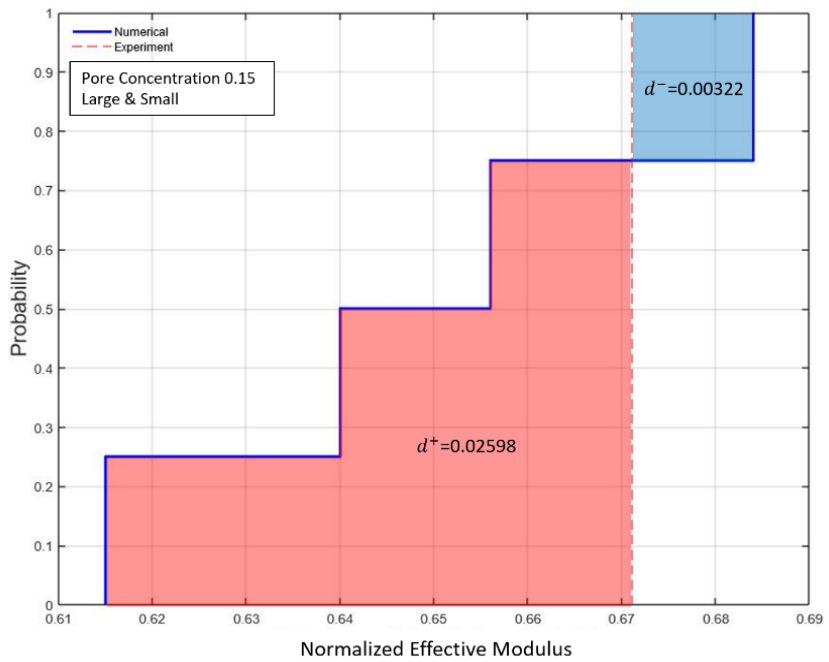
(b)

Figure 10   Empirical cumulative probability of the experimental data and simulation results of the models with (a) uniform circular pores and (b) non-uniform (large and small) circular pores, for the case of 0.20 pore concentration (see online version for colours)
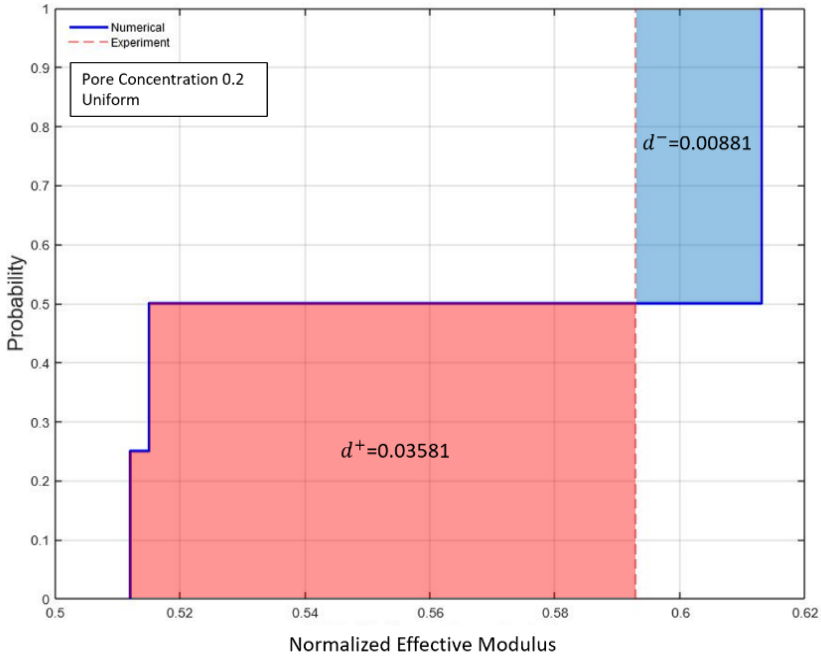
(a)
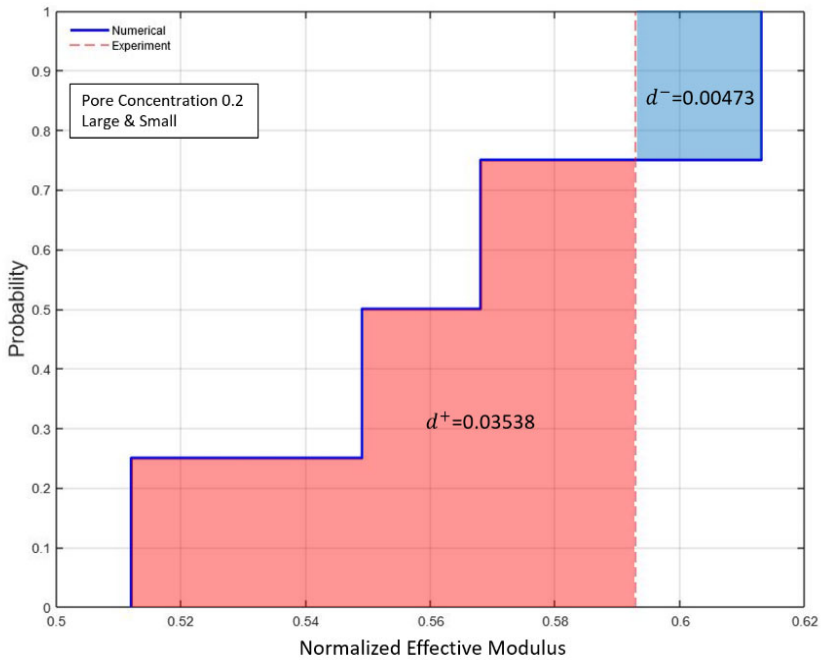
(b)

Figure 11 Overall model form uncertainty obtained from the empirical probability distribution mismatches between the experimental data and the simulation results presented in Figures 7–10 (see online version for colours)
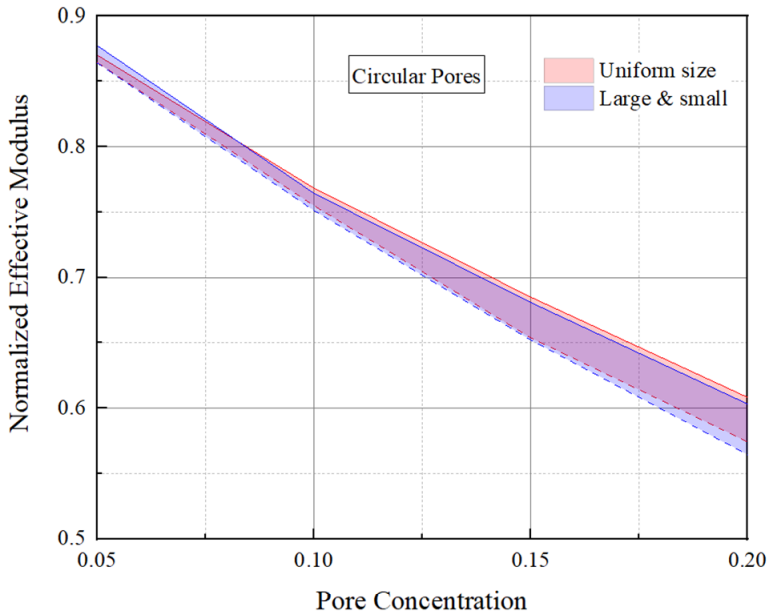
Attention is now turned to the local stress field developed in the pore-containing materials obtained from the numerical modelling. Figure 12 shows the contour plots of the normal stress component along the loading direction in the four circular pore models with a pore concentration of 0.1, when the overall applied tensile strain is 0.0001. This overall strain is well within the linear elastic regime where the local stress magnitudes scale linearly with the overall strain. Although the computation domains (the highlighted squares in Figure 1) are only a quarter of the repeated unit structure, in Figure 12, we display the full unit structures for better visualisation. It is evident that, in all cases, stress concentration occurs at the lateral edges of the pores. Directly above and below the pores, the ability of the solid matrix to carry the tensile stress is significantly reduced due to the 'traction-free' effect at the pore walls perpendicular to the loading axis. In the cases of the 0/90° loading, Figures 12(a) and 12(c), the largely unobstructed load path (primarily green colour) is in between the pores and generally parallel to the loading axis. In the cases of 45° loading, Figures 12(b) and 12(d), however, the load path appears to be along the diagonal directions connecting the stress concentration points at the pore edges. Contributions to the overall stress are less direct compared to the 0/90° loading, and thus the effective modulus is smaller for the 45° loading.

Figure 13 shows the contour plots of the normal stress components along the loading direction in the six elliptical pore models with a pore concentration of 0.1, when the overall applied tensile strain is 0.0001. The loading axis is indicated in each plot, and the stress fields presented are σ_{xx} for Figures 13(a) and 13(c) and σ_{yy} for the other parts. It can

be seen from Figures 13(a)–13(d) that stress concentration occurs at the lateral edges of the pores. However, when loading is along the minor axis of the ellipse, the stress concentration is more severe (with the locations at the sharper ends of the ellipse). This is the orientation for easier 'opening' of the elliptical voids, so the overall response is more compliant as seen in Figure 5(b). It is interesting to observe in Figure 13(e) that, in the case of aligned pores with mixed orientations, the vertically oriented pores show essentially no stress concentration. This is mainly due to the 'shielding' of the horizontally oriented pores aligned in the loading direction directly above and below. This effect does not exist for the staggered counterpart in Figure 13(f) where stress concentration occurs at all pores.

Figure 12   Contour plots of the normal stress component along the loading direction in the four circular pore models with the pore concentration of 10%, when the overall applied tensile strain is 0.0001, (a) uniform pore size under 0/90° loading (b) uniform pore size under 45° loading (c) large and small pore model under 0/90° loading (d) large and small pore model under 45° loading (see online version for colours)
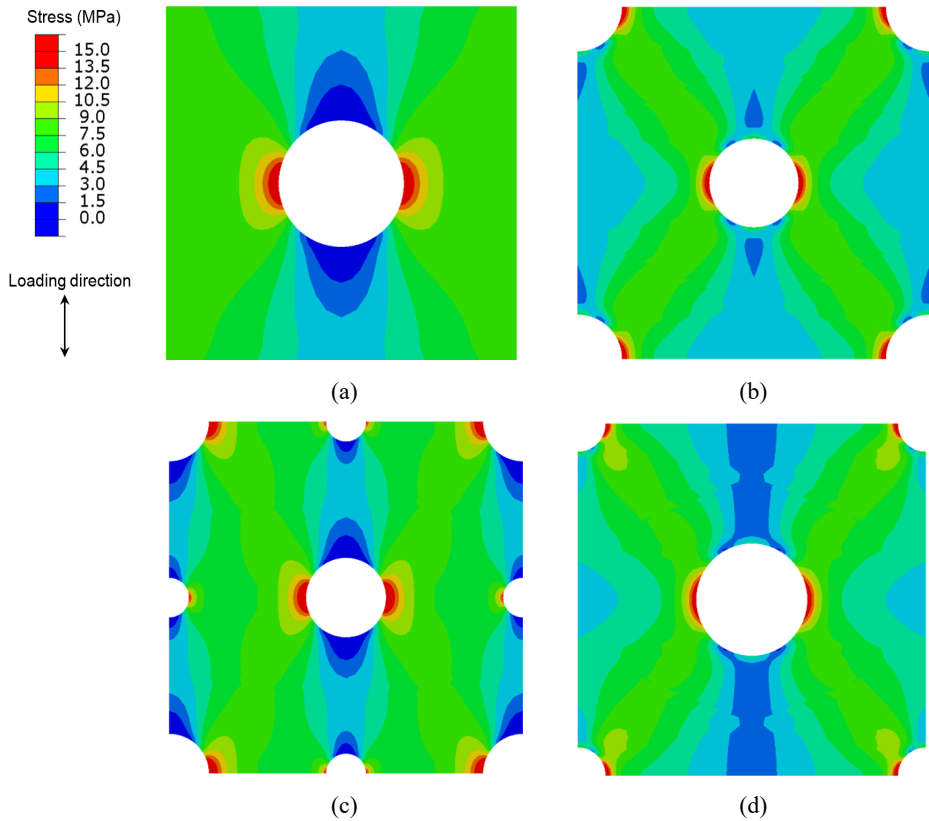
Note: For clarity purposes the entire periodic cells (instead of the quarter cells used for the computation highlighted in Figure 1) are included in the presentation.

Figure 13 Contour plots of normal stress in the tensile loading direction [σ_{xx} in (a) and (c) and σ_{yy} for the rest] in the six elliptical pore models with the pore concentration of 10%, when the overall applied tensile strain is 0.0001, (a) aligned pores with loading parallel to the major axis (b) aligned pores with loading parallel to the minor axis (c) staggered pores with loading parallel to the major axis (d) staggered pores with loading parallel to the minor axis (e) aligned mixed-orientation pores (f) staggered mixed-orientation pores (see online version for colours)
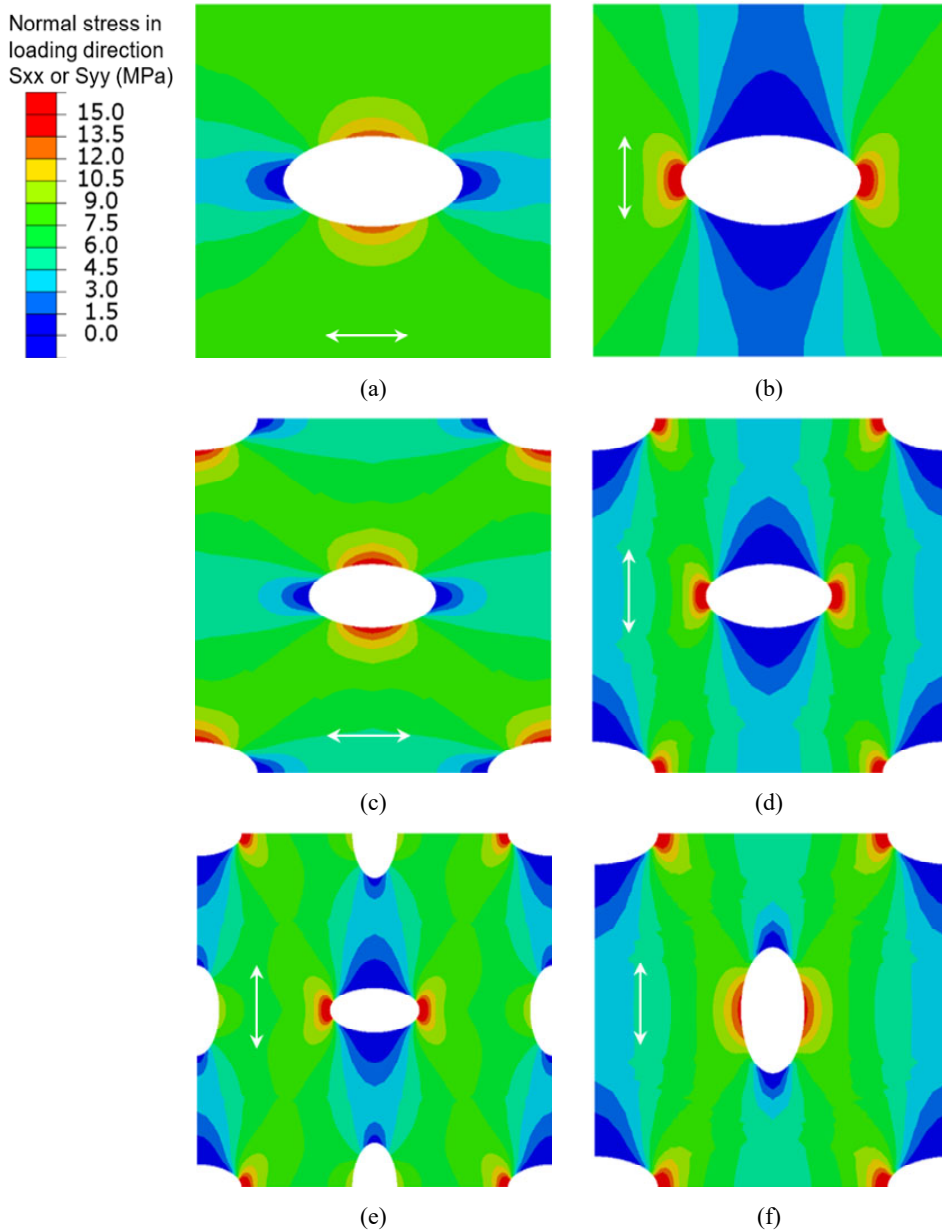
Notes: For clarity purposes, the entire periodic cells (instead of the quarter cells used for the computation highlighted in Figure 2) are included in the presentation. The loading directions are displayed as double arrows.

Figure 14   Simulated tensile stress-strain curves for models with 10% pore concentration, (a) the four circular pore models shown in Figure 1 (b) the six elliptical pore models shown in Figure 2 (see online version for colours)
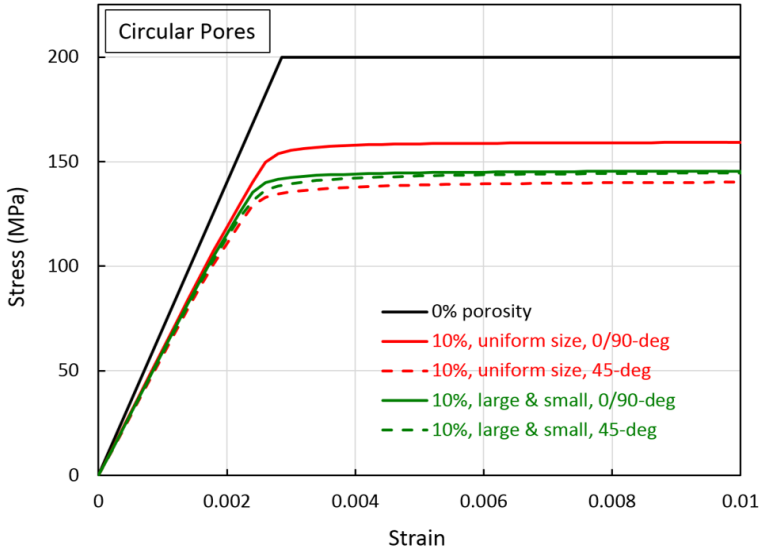
(a)
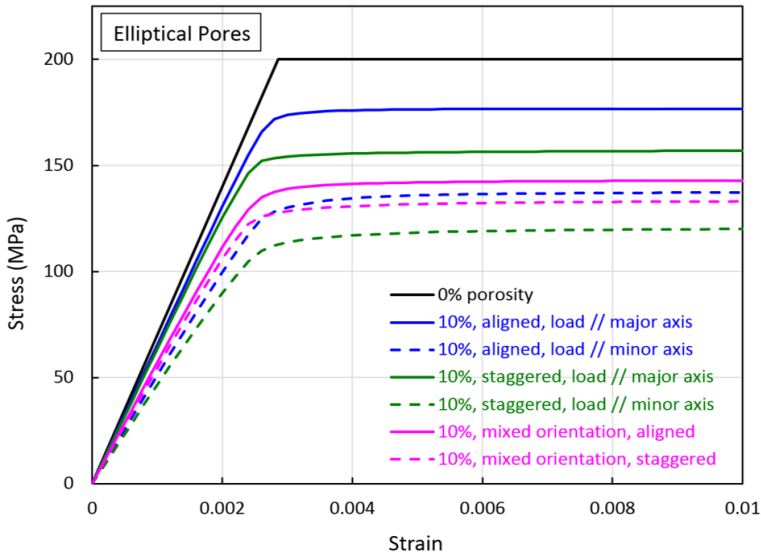
(b)

5   Effective plastic behaviour

We now consider the effective mechanical response well into the plastic regime. Figure 14(a) shows the simulated stress-strain curves for the four circular pore models,

using the 10% porosity as an example. As a reference, the stress-strain curve for the case of 0% porosity (pure matrix with the elastic-perfectly plastic behaviour) is included in Figure 14(a). It is evident that, with the existence of voids, the elastic-plastic transition becomes gradual, which is caused by the early localised yielding at the sites of stress concentration. As the plastic zone spreads to the entire matrix, a perfectly plastic response ensues. With the 10% porosity the overall plastic flow stress is much reduced compared to the yield strength of the pure matrix. The effective flow stress values for the four circular pore models actually follow the same order as effective modulus shown in Figure 5(a), with the 0/90° and 45° loadings of uniformly sized pore models being the highest and lowest, respectively. The combinations of large and small pores give rise to flow stresses in between.

Figure 15   Contour plots of the equivalent plastic strain in the four circular pore models with the pore concentration of 10%, when the overall applied tensile strain is 0.01, (a) uniform pore size under 0/90° loading (b) uniform pore size under 45° loading (c) large and small pore model under 0/90° loading (d) large and small pore model under 45° loading (see online version for colours)
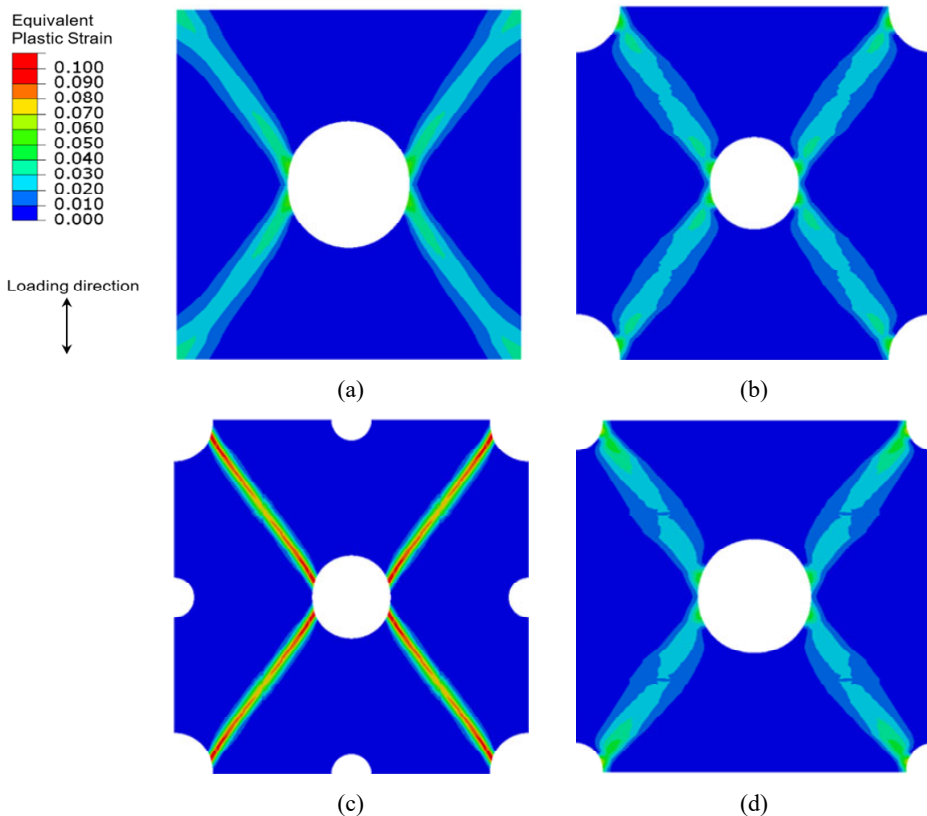
Note: For clarity purposes, the entire periodic cells (instead of the quarter cells used for the computation highlighted in Figure 1) are included in the presentation.

Figure 16   Contour plots of the equivalent plastic strain in the six elliptical pore models with the
pore concentration of 10%, when the overall applied tensile strain is 0.01, (a) aligned
pores with loading parallel to the major axis (b) aligned pores with loading parallel to
the minor axis (c) staggered pores with loading parallel to the major axis (d) staggered
pores with loading parallel to the minor axis (e) aligned mixed-orientation pores
(f) staggered mixed-orientation pores (see online version for colours)
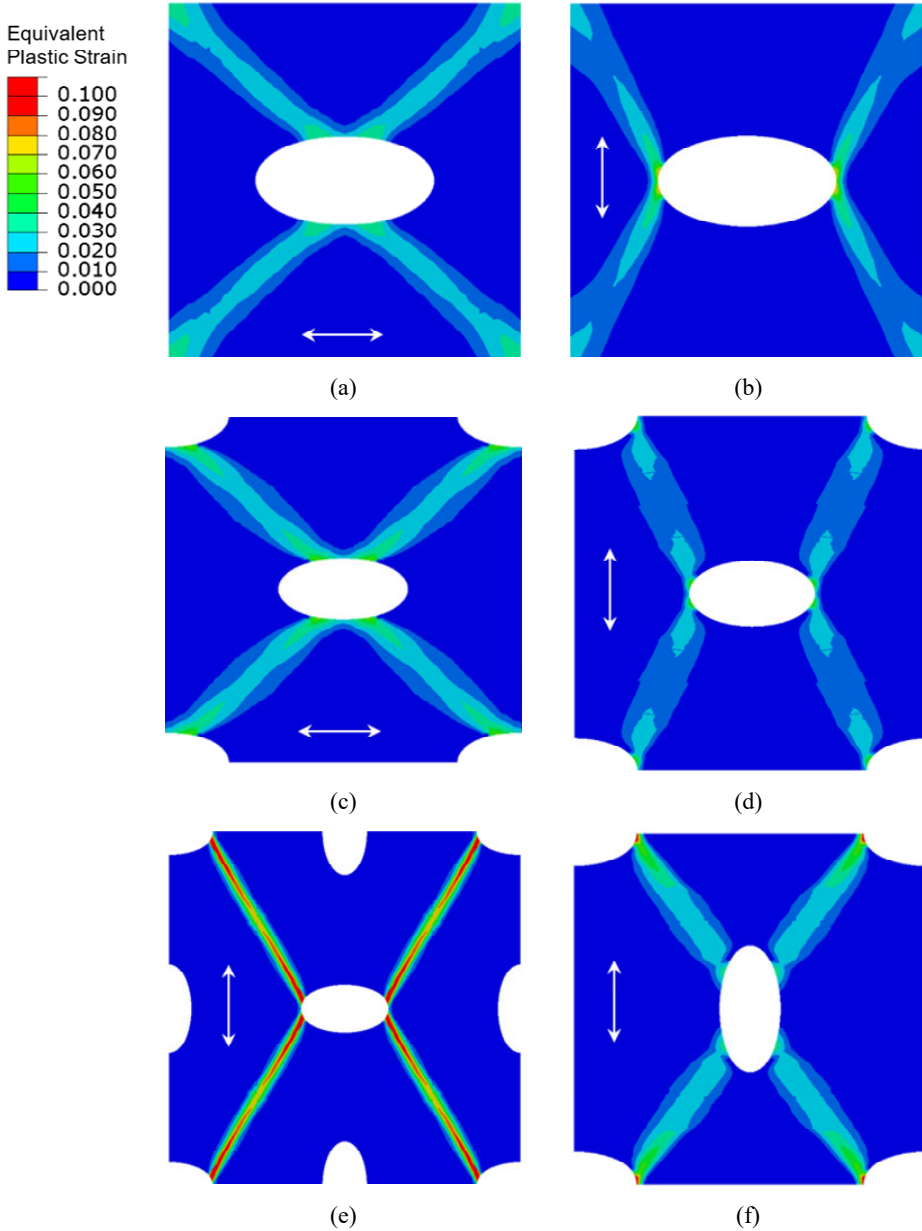
Notes: For clarity purposes, the entire periodic cells (instead of the quarter cells used for
the computation highlighted in Figure 2) are included in the presentation. The
loading directions are displayed as double arrows.

Figure 14(b) shows the simulated stress-strain curves for the six elliptical pore models, again using the 10% pore concentration as an example. As in the case of effective modulus, the plastic flow stress also displays a high degree of anisotropy, with loading along the major axis being much greater than that along the minor axis. The aligned arrangement also leads to a stronger stress-strain response than the staggered arrangement. While the flow stress levels among the six models do not strictly follow the order of the effective modulus (note the crossover of the blue and pink dashed curves), they are apparently strongly influenced by the elastic behaviour. A lower effective modulus generally leads to earlier yielding and then a lower plastic flow stress.

From the non-uniform stress fields presented in Figures 12 and 13 during elastic deformation, one can also expect a disturbed plastic flow field. Figure 15 shows the contour plots of equivalent plastic strain in the four circular pore models with a pore concentration of 10%, when the overall applied tensile strain is 0.01. Plastic deformation in a form of localised bands can be clearly seen (when there is no void, the homogeneous solid material displays a uniform plastic strain throughout.) The deformation bands appear to originate from the stress concentration sites and link up to become a network of plastic paths. In Figure 15(c) where large and small pores coexist, the 0/90° loading generates plastic deformation bands connecting only the large pores, with the small pores largely 'bypassed'. Also, the deformation bands are narrow with more intensive plastic strains, thus implying earlier damage initiation compared to other cases in real materials. When the same large/small pore model is undergoing 45° loading, Figure 15(d), all pores are involved in the banding process due to the geometric arrangement relative to the loading axis.

Figure 16 shows the contour plots of equivalent plastic strain in the six elliptical pore models with a pore concentration of 10%, when the overall applied tensile strain is 0.01. The loading axis is indicated in each plot. As in the cases of circular pores, distinct networks of plastic deformation bands linking the pores have formed. In Figure 16(e) with the mixed orientations of pores in the aligned arrangement, the vertically oriented ellipses are observed to be bypassed by the plastic bands. This is similar to the small circular pores in Figure 15(c); note that in Figure 13(e), these same vertically oriented elliptical pores are also missing the stress concentration due to the shielding effect discussed in the elastic deformation section. The narrow deformation bands in Figure 16(e) with enhanced plasticity again imply earlier damage initiation and thus reduced ductility in actual materials.

6   Conclusions

The current numerical study is devoted to the overall elastic-plastic behaviour of materials containing periodic arrays of pores up to 20% porosity. Experimental measurements were also conducted to validate the numerical findings for the elastic behaviour. It was found that the reduction of effective elastic modulus and plastic flow stress, compared to those of the pure solid matrix material, depend not only on the pore concentration but the spatial geometric arrangement of the pores. Under any fixed pore concentration, an aligned square array of pores (0/90° loading) results in a higher effective elastic modulus and higher plastic flow stress, compared to a staggered (45°) arrangement. The models with a combination of large and small circular pores fall between these extremes. Uniformly oriented elliptical pores give rise to anisotropy, with

loading parallel to the major (minor) elliptical axis leading to a stiffer (more compliant) and stronger (weaker) response. Depending on the geometric arrangement, not all pores actively participate in the deformation process. In a mixed and aligned configuration, the smaller circular pores and the elliptical pores oriented along the loading direction play an insignificant role; the discrete plastic deformation bands are sharper and largely bypass these pores. Earlier damage initiation and thus lower ductility can thus be expected.

Acknowledgements

References

Campillo, M., Pérez, P., Daher, J. and Pérez, L. (2021) 'Percentage porosity computation of three-dimensional non-convex porous geometries using the direct Monte Carlo simulation', *Engineering with Computers*, Vol. 37, No. 2, pp.951–973.

Christman, T., Needleman, A. and Suresh, S. (1989) 'An experimental and numerical study of deformation in metal-ceramic composites', *Acta Metallurgica*, Vol. 37, No. 11, pp.3029–3050.

Danes, F., Garnier, B. and Dupuis, T. (2003) 'Predicting, measuring, and tailoring the transverse thermal conductivity of composites from polymer matrix and metal filler', *International Journal of Thermophysics*, Vol. 24, No. 3, pp.771–784.

de Galarreta, S.R., Jeffers, J.R.T. and Ghouse, S. (2020) 'A validated finite element analysis procedure for porous structures', *Materials & Design*, Vol. 189, p.108546.

Digby, P.J. (1981) 'The effective elastic moduli of porous granular rocks', *Journal of Applied Mechanics*, Vol. 48, No. 4, pp.803–808.

Dinesh, B.V.S. and Bhattacharya, A. (2019) 'Effect of foam geometry on heat absorption characteristics of PCM-metal foam composite thermal energy storage systems', *International Journal of Heat and Mass Transfer*, Vol. 134, pp.866–883.

Doan, T., Le-Quang, H. and To, Q.D. (2020) 'Effective elastic stiffness of 2D materials containing nanovoids of arbitrary shape', *International Journal of Engineering Science*, Vol. 150, p.103234.

Gobetz, Z., Rowen, A., Dickman, C., Meinert, K. and Martukanitz, R. (2016) *Utilization of Additive Manufacturing for Aerospace Heat Exchangers*, Pennsylvania State University State College, USA.

Gu, S., Lu, T.J., Hass, D.D. and Wadley, H.N.G. (2001) 'Thermal conductivity of zirconia coatings with zig-zag pore microstructures', *Acta Materialia*, Vol. 49, No. 13, pp.2539–2547.

Hom, C.L. (1992) 'Three-dimensional finite element analysis of plastic deformation in a whisker-reinforced metal matrix composite', *Journal of the Mechanics and Physics of Solids*, Vol. 40, No. 5, pp.991–1008.

Ibrahim, Y., Elkholy, A., Schofield, J.S., Melenka, G.W. and Kempers, R. (2020) 'Effective thermal conductivity of 3D-printed continuous fiber polymer composites', *Advanced Manufacturing: Polymer & Composites Science*, Vol. 6, No. 1, pp.17–28.

Irick, K. and Fathi, N. (2019) 'Computational evaluation of thermal barrier coatings: two-phase thermal transport analysis', in *Verification and Validation*, American Society of Mechanical Engineers, May, Vol. 41174, p.V001T12A002.

Irick, K. and Fathi, N. (2020) 'Computational evaluation of thermal response of open-cell foam with circular pore', *Journal of Verification, Validation and Uncertainty Quantification*, DOI: 10.1115/1.4049323.

Kaviany, M. (1995) *Principles of Heat Transfer in Porous Media*, Springer, New York, NY.

Kırca, M., Gul, A., Ekinci, E., Yardım, F. and Mugan, A. (2007) 'Computational modeling of micro-cellular carbon foams', *Finite Elements in Analysis and Design*, Vol. 44, Nos. 1–2, pp.45–52.

Kozola, B.D. and Shen, Y-L. (2003) 'A mechanistic analysis of the correlation between overall strength and indentation hardness in discontinuously reinforced aluminum', *Journal of Materials Science*, Vol. 38, No. 5, pp.901–907.

Llorca, J., Needleman, A. and Suresh, S. (1991) 'An analysis of the effects of matrix void growth on deformation and ductility in metal-ceramic composites', *Acta Metallurgica et Materialia*, Vol. 39, No. 10, pp.2317–2335.

Oberkampf, W.L. and Roy, C.J. (2010) *Verification and Validation in Scientific Computing*, Cambridge University Press, Cambridge.

Pérez, L., Lascano, S., Aguilar, C., Estay, D., Messner, U., Figueroa, I.A. and Alfonso, I. (2015) 'DEM-FEA estimation of pores arrangement effect on the compressive Young's modulus for Mg foams', *Computational Materials Science*, Vol. 110, pp.281–286.

Pérez, L., Mercado, R. and Alfonso, I. (2017) 'Young's modulus estimation for CNT reinforced metallic foams obtained using different space holder particles', *Composite Structures*, Vol. 168, pp.26–32.

Ramakrishnan, N. and Arunachalam, V.S. (1990) 'Effective elastic moduli of porous solids', *Journal of Materials Science*, Vol. 25, No. 9, pp.3930–3937.

Renteria, A.F., Saruhan, B., Schulz, U., Raetzer-Scheibe, H.J., Haug, J. and Wiedenmann, A. (2006) 'Effect of morphology on thermal conductivity of EB-PVD PYSZ TBCs', *Surface and Coatings Technology*, Vol. 201, No. 6, pp.2611–2620.

Roy, C.J. and Voyles, I. (2013) 'Assessment of model validation approaches using the method of manufactured universes', in *ASME Verification and Validation Symposium*, May.

Shen, Y.L. (2010) *Constrained Deformation of Materials: Devices, Heterogeneous Structures and Thermo-mechanical Modeling*, Springer Science & Business Media, New York.

Shen, Y.L., Finot, M., Needleman, A. and Suresh, S. (1994) 'Effective elastic response of two-phase composites', *Acta metallurgica et materialia*, Vol. 42, No. 1, pp.77–97.

Shen, Y.L., Finot, M., Needleman, A. and Suresh, S. (1995) 'Effective plastic response of two-phase composites', *Acta metallurgica et materialia*, Vol. 43, No. 4, pp.1701–1722.

Sun, C.T. and Li, S. (1988) 'Three-dimensional effective elastic constants for thick laminates', *Journal of Composite Materials*, Vol. 22, No. 7, pp.629–639.

Uppu, S.K., Fathi, N., Shen, Y-L., Newell, P., Vorobieff, P. and Aleyasin, S.S. (2015) *Modeling and Simulation (M&S) Assessment of Mechanical Response of Open-cell Porous Media*, No. SAND2015-0585C.

Wilkins, T. and Shen, Y.L. (2001) 'Stress enhancement at inclusion particles in aluminum matrix composites: computational modeling and implications to fatigue damage', *Computational Materials Science*, Vol. 22, Nos. 3–4, pp.291–299.

Wu, S., Li, T., Tong, Z., Chao, J., Zhai, T., Xu, J., Yan, T., Wu, M., Xu, Z., Bao, H. and Deng, T. (2019) 'High-performance thermally conductive phase change composites by large-size oriented graphite sheets for scalable thermal energy harvesting', *Advanced Materials*, Vol. 31, No. 49, p.1905099.

Yeap, K.B., Kopycinska-Mueller, M., Chen, L., Chen, Y., Jungmann, M., Krause-Rehberg, R., Mahajan, S., Vlassak, J., Gall, M. and Zschech, E. (2013) 'The effect of the pore topology on the elastic modulus of organosilicate glasses', *Journal of Materials Research*, Vol. 28, No. 9, pp.1262–1268.

Zeng, T., Shao, J.F. and Xu, W.Y. (2015) 'A micromechanical model for the elastic-plastic behavior of porous rocks', *Computers and Geotechnics*, Vol. 70, pp.130–137.

Zhang, S., Lane, B., Whiting, J. and Chou, K. (2018) 'An investigation into metallic powder thermal conductivity in laser powder bed fusion additive manufacturing', in *Proc. Annu. Int. Solid Freefm. Fab. Symp.*, Austin, TX, November, Vol. 29, pp.1796–1807.

Zhao, J.J., Duan, Y.Y., Wang, X.D. and Wang, B.X. (2012) 'Experimental and analytical analyses of the thermal conductivities and high-temperature characteristics of silica aerogels based on microstructures', *Journal of Physics D: Applied Physics*, Vol. 46, No. 1, p.015304.

Zhao, Z., Zhang, H., Zou, G., Ren, H., Zhuang, W., Liu, L. and Zhou, Y.N. (2019) 'A predictive model for thermal conductivity of nano-Ag sintered interconnect for a SiC die', *Journal of Electronic Materials*, Vol. 48, No. 5, pp.2811–2825.

Zhu, W., Cai, X.N., Yang, L., Xia, J., Zhou, Y.C. and Pi, Z.P. (2019) 'The evolution of pores in thermal barrier coatings under volcanic ash corrosion using X-ray computed tomography', *Surface and Coatings Technology*, Vol. 357, pp.372–378.